





Sub-arc mantle fugacity shifted by sediment recycling across the Great Oxidation Event

Received: 27 January 2023

Accepted: 26 July 2023

Published online: 31 August 2023

 Check for updates

Hugo Moreira ^{1,2,8} ✉, Craig Storey ², Emilie Bruand ³, James Darling ², Mike Fowler ², Marine Cotte ^{4,5}, Edgar E. Villalobos-Portillo ⁴, Fleurice Parat¹, Luís Seixas ⁶, Pascal Philippot ^{1,7} & Bruno Dhuime ¹

The chemical exchange between the atmosphere, crust and mantle depends on sediment recycling via subduction. However, it remains unclear how atmospherically modified sediment may affect mantle oxygen fugacity through time. The Great Oxidation Event, among the most important atmospheric changes on Earth, offers an opportunity to investigate changes in magmatism related to surface–mantle interactions. Here we use sulfur K-edge micro X-ray absorption near-edge structure spectroscopy to measure the relative abundances of S⁶⁺, S⁴⁺ and S²⁻ state in apatite inclusions hosted in 2.4–2.1-billion-year-old igneous zircons from the Mineiro Belt, Brazil. The host magmas record intracrustal melting of juvenile crust and the involvement of recycled sediments in the sub-arc mantle wedge. Unaltered apatite inclusions reveal a change from reduced to more oxidized magmas from pre- to post-Great Oxidation Event during the early Proterozoic. We argue that this change is a direct result of deep subduction of oxidized sediments and thus evidence of mantle–atmosphere interaction across the Great Oxidation Event. This suggests that the onset of sediment recycling in the Archaean provided atmospheric access to the mantle, and early ‘whiffs’ of oxygen may have already contributed to a localized increase of calc-alkaline magmatism and related ore deposits on Earth.

Substantial accumulation of free oxygen in the atmosphere occurred between ~2.45 and 2.20 billion years ago (Ga) (refs. 1–3), with permanent atmospheric oxygenation between 2.3 and 2.2 Ga (refs. 4,5). This period is known as the Great Oxidation Event (GOE) and marks the most dramatic change in Earth’s surface chemistry and habitability⁶. However, it remains unclear if these major atmospheric changes affected the amount of free or chemically available oxygen in the mantle and, consequently, the redox state of mantle-derived magmas. In the modern Earth, considerable amounts of surface-oxidized components infiltrate the mantle via slab fluids and subducted sediments⁷, ultimately influencing the oxidation state of the mantle wedge and arc magmas^{8,9}.

A better understanding of how magmas changed oxidation through time would clarify ocean–atmosphere influence on mantle redox potential and whether deep-ocean oxygenation is a feature restricted to the Phanerozoic^{10,11}.

Mantle oxygen fugacity (f_{O_2}) probably changed in the early Earth as a result of metallic Fe retention during core formation and further homogenization^{12,13}, but subsequent variations through time are debatable. The mantle f_{O_2} is either described as largely unchanged^{14–16} or overall having a near-constant rate of increase through time^{17–20}.

Common explanations for the absence of identifiable f_{O_2} change in the mantle are based on the ‘infinite reservoir’ argument, given its

¹Géosciences Montpellier, Université de Montpellier, CNRS, Montpellier, France. ²School of the Environment, Geography and Geosciences, University of Portsmouth, Portsmouth, UK. ³Geo-Ocean, CNRS, Université de Bretagne Occidentale, Ifremer, Brest, France. ⁴European Synchrotron Radiation Facility, Grenoble, France. ⁵Laboratoire d’Archéologie Moléculaire et Structurale, University of Sorbonne, Paris, France. ⁶Departamento de Engenharia de Minas, Universidade Federal de Ouro Preto, Ouro Preto, Brazil. ⁷Departamento de Geofísica, Astronomia e Ciências Atmosféricas, Universidade de São Paulo, São Paulo, Brazil. ⁸Present address: Géosciences Montpellier, Université de Montpellier, CNRS, Montpellier, France. ✉e-mail: hugo.moreira@umontpellier.fr

relatively larger size compared to surface reservoirs (that is, atmosphere, hydrosphere and crust^{6,15}). Nonetheless, mid-ocean ridge basalts show an increase in the Archaean potentially linked to early ‘whiffs’ of atmospheric oxygen¹⁸, suggesting that the upper mantle can be affected by changes in the atmosphere. However, despite evidence for recycling of continental materials during at least the past 3.0 Gyr (for example, ref. 21), it is unclear how much this has affected the redox state of the mantle, even across the GOE. Here we test the hypothesis of a change in the redox state of magmas in the sub-arc mantle region via recycling processes akin to subduction during the Palaeoproterozoic.

Oxygen fugacity and recycling in the geological record

One of the recognizable changes in the magma record that can provide insights into surface–mantle interactions is the transition from tonalite–trondhjemite–granodiorite (TTG) to sanukitoid magmas recorded in most cratons worldwide^{22,23}. This transition started in the Palaeoarchaean and progressed with reduced occurrence to the Palaeoproterozoic^{22,24,25}. TTGs are formed by partial melting at depth of (often) altered basaltic rocks, whereas sanukitoids require interaction of TTG such as melts and/or sediments within a metasomatized mantle wedge^{22,26}. Sanukitoid petrogenesis thus constitutes *prima facie* evidence for crustal recycling into the upper mantle via ‘subduction’²⁷. The tectonic settings for this secular magmatic transition are still debated^{23,28,29}, but all models involve a mechanism that includes a return to the mantle of material that was previously at the Earth’s surface (for example, ref. 30).

Magmas can contain sulfur in variable valence states (S^{2-} , S^0 , S^{4+} , S^{6+}), which are chiefly controlled by melting conditions and assimilation of surface material at source^{31,32}. The preferential assimilation and fugacity variation of sulfur from mantle source to crustal emplacement is controlled by crystallization and/or degassing of the magma³³. As a result, whole-rock analyses of sulfur speciation may involve a large uncertainty due to the volatility and instability of sulfur during and, especially, after crystallization. This problem is greatly reduced when melt or mineral phase inclusions are analysed as they are protected by the host crystals and therefore more likely to preserve pristine speciation through subsequent tectono-metamorphic-hydrothermal events^{34,35}.

The accessory mineral apatite has great potential to record sulfur speciation as it can seamlessly incorporate both reduced and oxidized sulfur^{36,37} and so retain a proxy for the oxygen fugacity of the crystallizing magma^{38,39}. Unfortunately, apatite grains easily recrystallize when the host rock is affected by hydrothermal fluids and/or deformation. Hence our approach includes analysing the sulfur speciation of apatite inclusions shielded in host zircon grains and of apatite grains present in the rock’s matrix. This avoids secondary alteration processes and offers a robust way to monitor the redox state of the primary magmas (for example, refs. 40–42). Importantly, U–Pb–Hf isotopes of the host zircon can be used to provide information on the age and the source (that is, mantle or crustal origin) of the magma from which they crystallized⁴³, and stable oxygen isotopes can identify a supracrustal component and aqueous alteration at varying temperatures^{44,45}. Zircon trace element analyses can also provide insights into the composition and redox state of host magmatic rocks⁴⁶. Thus, combining a multi-isotopic and elemental study of zircon host minerals with extra information on the sulfur speciation of its apatite inclusions is a robust approach to study redox changes in magmas, applied here to those which are primary components of the continental crust.

A Palaeoproterozoic magmatic transition

We investigate samples from two well-characterized suites of intermediate granitoids from the juvenile Mineiro Belt, Brazil. These magmatic suites were classified as a 2.35 Ga TTG and 2.13 Ga sanukitoid based on

field evidence, geochemistry and isotope studies, both in whole-rock and accessory phases^{24,47–49}. They are particularly suitable for this study because they record the youngest transition from TTG to sanukitoid magmatism on Earth, taking place in the Palaeoproterozoic rather than in the Archaean as in many other cratons^{23,24}. The transition started shortly before the global ‘tectono-magmatic lull’⁵⁰ and evolved across the time period of irreversible oxygenation of Earth’s atmosphere⁵.

Isotopically, both whole-rock and individual zircon analyses show that the TTGs plot above the chondritic reservoir value (CHUR) and that the sanukitoids have approximately chondritic values^{24,49}. This indicates that both magmatic suites have a ‘juvenile’ signature⁴³. Moreover, a projected crustal evolution line typical of granitic crust ($^{176}\text{Lu}/^{177}\text{Hf} = 0.01$) demonstrates that the sanukitoid suite can be traced back 200 Myr to the TTG composition, and in turn, those two can be traced back to a depleted mantle (DM) source at around 2.5 Ga (Fig. 1a). Thus, shortly (150 Myr) after mantle extraction, the mafic parental source first underwent partial melting and generated the 2.35-Gyr-old TTGs⁴⁸. A similar mafic source was remelted about 200 Myr later⁴⁷, but this time the magmas record increased depth of melting, as a result of steepening of the subducted slab and opening of a mantle wedge²⁴. This second stage generated 2.13 Ga sanukitoid magmas that contain abundant mafic enclaves, with geochemical and oxygen isotope analyses suggesting the involvement of sediments²⁴ (Fig. 1b). The absence of any zircon inheritance and chondritic zircon $\epsilon\text{Hf}(t)$ values ($^{176}\text{Hf}/^{177}\text{Hf}$ ratios relative to chondrite at the time of crystallization) alongside substantial range in zircon $\delta^{18}\text{O}$ (+4.7‰ to +7.5‰ deviation from the $^{18}\text{O}/^{16}\text{O}$ ratio of the Vienna Standard Mean Ocean Water) suggests that crustal assimilation is unlikely and the sediments originated from the 2.13 Ga magmatic arc itself—a geological phenomenon described as a ‘self-feeding arc’, where arc sediments form, are deposited in the adjacent ocean and then are subducted²⁴ (Fig. 1c). The high concentration of elements that are strongly mobile in aqueous fluids (for example, Ba and Sr > 1,000 ppm) alongside enrichment in mantle-compatible elements (Mg number: -55, Ni: -80 ppm and Cr: -200 ppm; ref. 47) strongly support sediment admixture in the sub-arc mantle wedge, where sanukitoid magmas were sourced.

The magmas described above evolved within a geologically short duration (2.5–2.35–2.13 Ga) in an environment akin to intra-oceanic arcs and away from continental sources. Their evolution was nonetheless long enough to witness variations in atmospheric oxygenation consequent upon the GOE. In this context, the intrinsic relationship of the suites as derived from a similar basaltic source remelted at different geological intervals^{47–49} suggests that comparative changes of fugacity are feasible.

Sulfur speciation in matrix apatite and inclusions

We have determined the valence(s) of sulfur in apatite using the X-ray absorption near-edge structure (μ -XANES) technique at the European Synchrotron Radiation Facility (ESRF) in Grenoble, France (Methods and Supplementary Data). We present 40 analyses in 26 matrix apatite grains and 136 analyses in 20 apatite inclusions in zircons. For all studied samples, we targeted crack-free apatite inclusions that show no crystallographic misorientation and display a ‘hotspot’ zone in sulfur concentration maps (Fig. 2). The patterns show higher sulfur concentration in the centre of the inclusions and gradual decrease towards the host zircon crystal. This core-to-rim zonation is taken to represent sulfur incorporation and retention during early crystallization and thus records primary signatures of the crystallizing magma. It is unlikely that they represent sulfur exchange with the host, as zircon has negligible sulfur content and extremely slow diffusion rates⁵¹.

Although many apatite inclusions from the 2.35-Gyr-old TTG suite have proven to be sulfur barren, six inclusions and a few matrix apatites have sufficiently high sulfur to yield measurable μ -XANES spectra (Fig. 2); these show remarkably lower S^{6+}/S_{TOTAL} (that is, they have dominant S^{2-} peak) compared to the apatite sulfur speciation in the

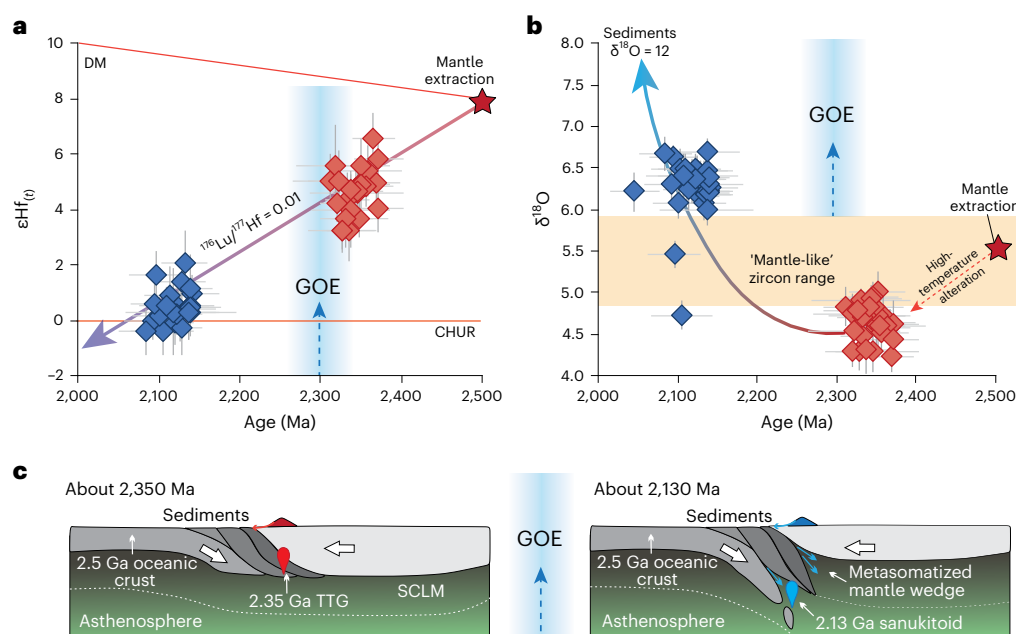


Fig. 1 | Palaeoproterozoic TTG–sanukitoid magmatic transition. **a**, Zircon U–Pb ages versus $^{176}\text{Hf}/^{177}\text{Hf}(t)$ ratios (expressed as $\epsilon\text{Hf}(t)$ values relative to chondrite at the time of crystallization t). Zircons from TTG magmas ($n = 31$) have significantly positive $\epsilon\text{Hf}(t)$, whereas zircons from the sanukitoid magmas ($n = 33$) are near the CHUR. A crustal evolution line links both suites of rocks to a DM melting event at 2.5 Ga. **b**, Zircon $^{18}\text{O}/^{16}\text{O}$ ratios (expressed as $\delta^{18}\text{O}$ relative to Vienna Standard Mean Ocean Water) show that the basaltic crust was hydrothermally altered

at high temperature ($\sim 4.5\%$) before generating TTG magmas at 2.35 Ga and before remelting in the metasomatized mantle wedge at 2.13 Ga. The latter event generated sanukitoids that have zircons with heavier oxygen ($\sim 6.5\%$). Individual error bars in **a** and **b** are shown at 2 standard errors. **c**, Tectonic model for the generation of magmas in the Palaeoproterozoic pre- and post-GOE peak. SCLM stands for subcontinental lithospheric mantle.

2.13 Ga sanukitoid (Fig. 3). Matrix apatites and three out of six inclusions have much larger uncertainties and $\text{S}^{6+}/\text{S}_{\text{TOTAL}}$ between 0.4 and 0.7, while analyses of the other inclusions show $\text{S}^{6+}/\text{S}_{\text{TOTAL}} < 0.1$ (Fig. 3). As matrix apatites are more prone to recrystallization for not being shielded in zircon, we suggest that these three inclusions with much higher $\text{S}^{6+}/\text{S}_{\text{TOTAL}}$ were affected by post-crystallization interaction with fluids in relative higher fugacity. Moreover, these inclusions with higher $\text{S}^{6+}/\text{S}_{\text{TOTAL}}$ have no detectable ‘hotspot’ zoning, indicating sulfur redistribution or concentrations straddling the detection limit. One of the analysed inclusions with very low $\text{S}^{6+}/\text{S}_{\text{TOTAL}}$ is hosted by a zircon grain that contains an ilmenite inclusion, reinforcing the interpretation of magmatic crystallization under possible reduced conditions (Fig. 2). Ilmenite and magnetite occur in the matrix, but magnetite is thought to have been produced during recrystallization of the host rock during deformation/metamorphism⁴⁸, a process that apparently did not affect the armoured inclusions.

Our results show that matrix apatite grains from the 2.13 Gyr sanukitoid depict a conspicuous oxidized pattern with dominant S^{6+} and high $\text{S}^{6+}/\text{S}_{\text{TOTAL}}$ peak area ratio that is in agreement with apatite inclusions from the same sample (Fig. 2). The high $\text{S}^{6+}/\text{S}_{\text{TOTAL}}$ for both inclusions and apatite grains in the rock matrix suggests that if any recrystallization event has occurred, it was similarly oxidizing if compared to the primary fugacity of the inclusions (Fig. 3). Moreover, magnetite is a common opaque mineral phase in these rocks, formed as isometric homogeneous crystals included in hornblende⁴⁷, which overall points towards primary oxidizing crystallization conditions.

Quantifying changes in oxygen fugacity

To determine f_{O_2} and ascertain the magnitude of change, we used a sulfur-in-apatite experimental calibration oxybarometer that combines the fayalite–magnetite–quartz buffer (FMQ) and $\text{S}^{6+}/\text{S}_{\text{TOTAL}}$ (ref. 39) (Fig. 3a). Additionally, we used trace element analyses of the host zircons in a proxy that correlates zircon composition to oxygen

fugacity relative to FMQ⁴⁶. The f_{O_2} distance from the FMQ buffer (ΔFMQ) is then plotted against the zircon U/Yb to relate to sediment input at the source and/or crustal contamination of the magmas⁵² (Fig. 3b).

Our results demonstrate that the isotopically and petrologically linked TTG and sanukitoid suites in the Mineiro Belt of Brazil crystallized under different redox conditions (Fig. 3). The 2.35-Gyr-old TTG formed when atmospheric oxygen levels fluctuated across a threshold of 10^{-5} of present atmospheric levels⁵³ and primary apatite inclusions are reduced, with the three most precise measurements ranging from $\Delta\text{FMQ} -0.75 \pm 0.30$ to -0.28 ± 0.38 (2σ standard deviation—average of several analyses within each inclusion; Fig. 3a). The younger 2.13-Gyr-old sanukitoid post-dates the GOE when atmospheric oxygen levels stabilized permanently between 0.1 and 40% present atmospheric levels⁵⁴, and primary inclusions show oxidized sulfur speciation ranging from $\Delta\text{FMQ} + 0.80 \pm 0.16$ to $+1.24 \pm 0.36$ (Fig. 3a). Despite some intergrain variation, trace element analyses in zircons confirm that the 2.13-Gyr-old sanukitoid suite is more oxidized than the 2.35-Gyr-old TTG and corroborates the sulfur speciation data in apatite inclusions (Fig. 3b). The higher U/Yb in zircons from the sanukitoid suite is in agreement with elevated $\delta^{18}\text{O}$ and is attributed to surface-derived oxidized sediments that metasomatized the mantle.

An atmospheric window to the mantle

Modern marine sediments can be highly oxidized compared to upper mantle-derived basalts⁸. Their subduction will carry this surficial redox signature and affect the oxidation state of modern arc magmas⁷⁹. The generation of a deep subduction-like setting in the Palaeoproterozoic would have facilitated sediment input into the sub-arc mantle source ($>10\%$ by volume)²⁴. These sediments may have carried sulfate and ferric iron into the mantle wedge in a similar way to that observed in Phanerozoic arcs^{10,11}. Oxidized sanukitoid magmas were then formed at 2.13 Ga during melting of a 2.5-Gyr-old altered oceanic slab and its sedimentary carapace (Fig. 1). We suggest that this change in tectonic

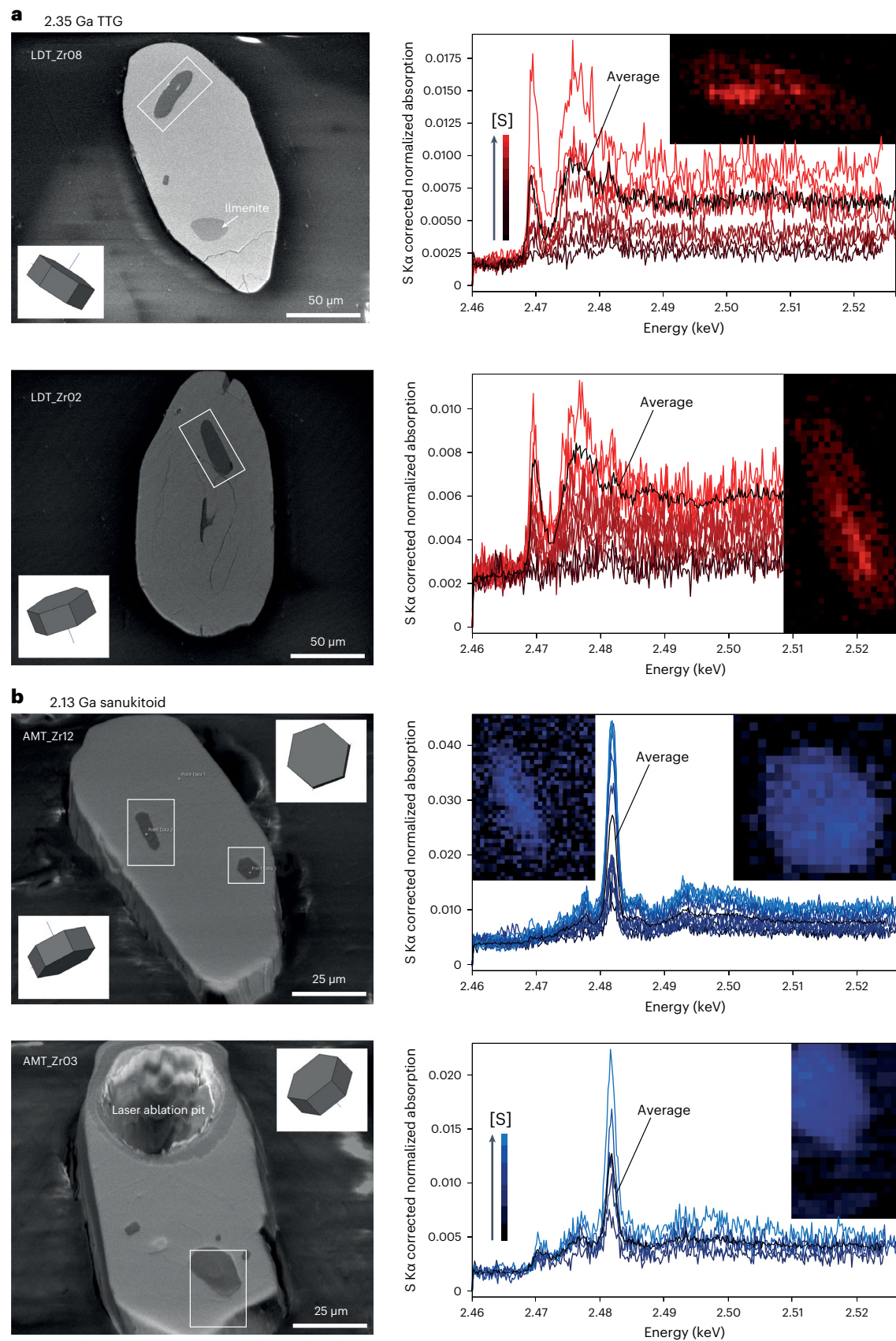


Fig. 2 | Backscattered electron images of inclusions in zircon and sulfur speciation spectra. a–b, Twenty-nine μ -XANES analyses in six apatite inclusions from the TTG sample and 108 analyses in 14 inclusions from the sanukitoid sample show that the average spectra differ greatly from a reduced (high

S^{2-}) speciation in TTG host zircons (a) to an oxidized speciation (high S^{6+}) in sanukitoid host zircons (b). Inset diagrams show the crystallographic orientation of the inclusions and their relative sulfur concentration. Sample labels are indicated in the top left corner of each image.

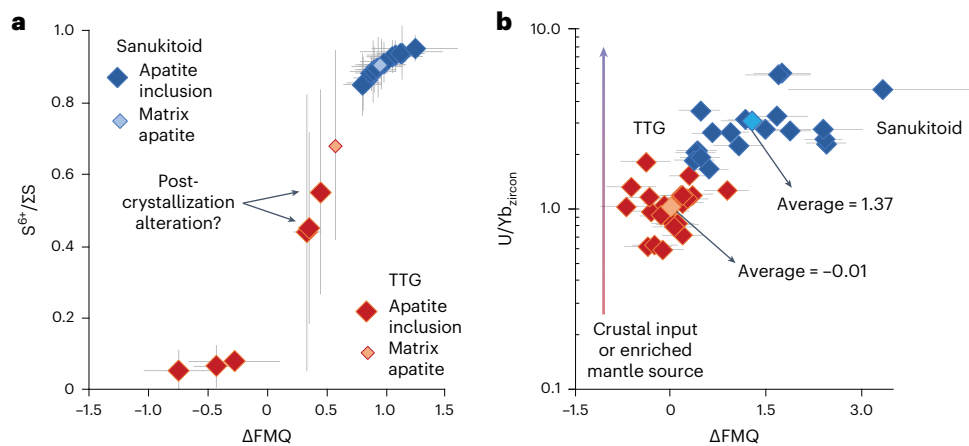


Fig. 3 | Oxygen fugacity of the samples studied with respect to the fayalite-magnetite-quartz buffer. a, ΔFMQ calculated via $S^{6+}/\Sigma S_{TOTAL}$ oxybarometer proxy. Large dark diamonds are averages of μ -XANES analyses within a single inclusion (sample size as indicated in Fig. 2 caption). Averages of 15 and 25 analyses, respectively, in six matrix apatite grains from the TTG sample (red) and

20 from the sanukitoid samples (blue) are plotted as smaller lighter diamonds. Error bars are 2 standard deviations. **b**, ΔFMQ calculated via zircon trace element proxy versus U/Yb ratios of individual zircon grains from sanukitoid ($n = 20$) and TTG ($n = 23$) samples. Error bars are 2 standard errors.

style allowed the atmosphere to dramatically influence sub-arc mantle chemistry through transfer of oxidized sediments (for example, refs. 7,9). The fortuitous occurrence of a TTG-sanukitoid transition in the Mineiro Belt across the GOE has allowed this change in oxidation state to be observed.

The global TTG-sanukitoid transitional record characterizes vigorous and protracted crustal recycling and mantle metasomatism in the early Earth (for example, refs. 22,26). Although localized and with less magnitude than the GOE, Archaean 'whiffs' of oxygen may have similarly altered the nature of subducted sediments⁵⁵ and started to modify the oxygen fugacity of mantle sources in the Archaean (compare with ref. 42). It then suggests that similar mantle-surface interactions could have had a major influence on magmatism and metallogenic endowment since the Archaean⁵⁶ and that the oxidation of the mantle was diachronous and related to the onset of global plate tectonics. The subsequent irreversible step-rise of oxygen in the Palaeoproterozoic may have led to the dominance of characteristically oxidized calc-alkaline magmas in the geological record.

Online content

Any methods, additional references, Nature Portfolio reporting summaries, source data, extended data, supplementary information, acknowledgements, peer review information; details of author contributions and competing interests; and statements of data and code availability are available at <https://doi.org/10.1038/s41561-023-01258-4>.

References

- Philippot, P. et al. Globally asynchronous sulphur isotope signals require re-definition of the Great Oxidation Event. *Nat. Commun.* **9**, 2245 (2018).
- Warke, M. R. et al. The great oxidation event preceded a paleoproterozoic 'snowball Earth'. *Proc. Natl Acad. Sci. USA* **117**, 13314-13320 (2020).
- Izon, G. et al. Bulk and grain-scale minor sulfur isotope data reveal complexities in the dynamics of Earth's oxygenation. *Proc. Natl Acad. Sci. USA* **119**, e2025606119 (2022).
- Luo, G. et al. Rapid oxygenation of Earth's atmosphere 2.33 billion years ago. *Sci. Adv.* **2**, e1600134 (2016).
- Poulton, S. W. et al. A 200-million-year delay in permanent atmospheric oxygenation. *Nature* **592**, 232-236 (2021).
- Lee, C. T. A. et al. Two-step rise of atmospheric oxygen linked to the growth of continents. *Nat. Geosci.* **9**, 417-424 (2016).
- Ague, J. J. et al. Slab-derived devolatilization fluids oxidized by subducted metasedimentary rocks. *Nat. Geosci.* **15**, 320-326 (2022).
- Kelley, K. A. & Cottrell, E. Water and the oxidation state of subduction zone magmas. *Science* **325**, 605-607 (2009).
- Padrón-Navarta, J. A., López Sánchez-Vizcaíno, V., Menzel, M. D., Gómez-Pugnaire, M. T. & Garrido, C. J. Mantle wedge oxidation from deserpentinization modulated by sediment-derived fluids. *Nat. Geosci.* **16**, 268-275 (2023).
- Brounce, M., Kelley, K. A., Cottrell, E. & Reagan, M. K. Temporal evolution of mantle wedge oxygen fugacity during subduction initiation. *Geology* **43**, 775-778 (2015).
- Stolper, D. A. & Bucholz, C. E. Neoproterozoic to early Phanerozoic rise in island arc redox state due to deep ocean oxygenation and increased marine sulfate levels. *Proc. Natl Acad. Sci. USA* **116**, 8746-8755 (2019).
- Frost, D. J. & McCammon, C. A. The redox state of Earth's mantle. *Annu. Rev. Earth Planet. Sci.* **36**, 389-420 (2008).
- O'Neill, C. & Aulbach, S. Destabilization of deep oxidized mantle drove the Great Oxidation Event. *Sci. Adv.* **8**, eabg1626 (2022).
- Canil, D. Vanadium partitioning and the oxidation state of Archaean komatiite magmas. *Nature* **389**, 842-845 (1997).
- Li, Z. X. A. & Lee, C. T. A. The constancy of upper mantle fO_2 through time inferred from V/Sc ratios in basalts. *Earth Planet. Sci. Lett.* **228**, 483-493 (2004).
- Williams, H. M., Wood, B. J., Wade, J., Frost, D. J. & Tuff, J. Isotopic evidence for internal oxidation of the Earth's mantle during accretion. *Earth Planet. Sci. Lett.* **321**, 54-63 (2012).
- Kadoya, S., Catling, D. C., Nicklas, R. W., Puchtel, I. S. & Anbar, A. D. Mantle data imply a decline of oxidizable volcanic gases could have triggered the Great Oxidation. *Nat. Commun.* **11**, 2774 (2020).
- Aulbach, S. & Stagno, V. Evidence for a reducing Archean ambient mantle and its effects on the carbon cycle. *Geology* **44**, 751-754 (2016).
- Nicklas, R. W., Puchtel, I. S. & Ash, R. D. Redox state of the Archean mantle: evidence from V partitioning in 3.5-2.4 Ga komatiites. *Geochim. Cosmochim. Acta* **222**, 447-466 (2018).
- Gao, L. et al. Oxidation of Archean upper mantle caused by crustal recycling. *Nat. Commun.* **13**, 3283 (2022).
- Dhuime, B., Hawkesworth, C. J., Cawood, P. A. & Storey, C. D. A change in the geodynamics of continental growth 3 billion years ago. *Science* **335**, 1334-1336 (2012).

22. Martin, H., Moyen, J. F. & Rapp, R. The sanukitoid series: magmatism at the Archaean–Proterozoic transition. *Earth Environ. Sci. Trans. R. Soc. Edinb.* **100**, 15–33 (2009).
23. Laurent, O., Martin, H., Moyen, J. F. & Doucelance, R. The diversity and evolution of late-Archaean granitoids: evidence for the onset of ‘modern-style’ plate tectonics between 3.0 and 2.5 Ga. *Lithos* **205**, 208–235 (2014).
24. Moreira, H., Storey, C., Fowler, M., Seixas, L. & Dunlop, J. Petrogenetic processes at the tipping point of plate tectonics: Hf–O isotope ternary modelling of Earth’s last TTG to sanukitoid transition. *Earth Planet. Sci. Lett.* **551**, 116558 (2020).
25. Bruno, H. et al. Neoproterozoic and Rhyacian TTG–Sanukitoid suites in the southern São Francisco Palecontinent, Brazil: evidence for diachronous change towards modern tectonics. *Geosci. Front.* **11**, 1763–1787 (2020).
26. Nebel, O. et al. When crust comes of age: on the chemical evolution of Archaean, felsic continental crust by crustal drip tectonics. *Phil. Trans. R. Soc. A* **376**, 20180103 (2018).
27. Fowler, M. & Rollinson, H. Phanerozoic sanukitoids from Caledonian Scotland: implications for Archaean subduction. *Geology* **40**, 1079–1082 (2012).
28. Martin, H. & Moyen, J. F. Secular changes in tonalite-trondhjemite-granodiorite composition as markers of the progressive cooling of Earth. *Geology* **30**, 319–322 (2002).
29. Smithies, R. H. et al. Oxygen isotopes trace the origins of Earth’s earliest continental crust. *Nature* **592**, 70–75 (2021).
30. Bédard, J. H. Stagnant lids and mantle overturns: implications for Archaean tectonics, magmagenesis, crustal growth, mantle evolution, and the start of plate tectonics. *Geosci. Front.* **9**, 19–49 (2018).
31. Métrich, N. & Mandeville, C. W. Sulfur in magmas. *Elements* **6**, 81–86 (2010).
32. Brounce, M., Boyce, J. W. & McCubbin, F. M. Sulfur in apatite from the Nakhla meteorite record a late-stage oxidation event. *Earth Planet. Sci. Lett.* **595**, 117784 (2022).
33. Parat, F., Holtz, F. & Klügel, A. S-rich apatite-hosted glass inclusions in xenoliths from La Palma: constraints on the volatile partitioning in evolved alkaline magmas. *Contrib. Mineral. Petrol.* **162**, 463–478 (2011).
34. Métrich, N. & Clocchiatti, R. Sulfur abundance and its speciation in oxidized alkaline melts. *Geochim. Cosmochim. Acta* **60**, 4151–4160 (1996).
35. Meng, X. et al. Oxidized sulfur-rich arc magmas formed porphyry Cu deposits by 1.88 Ga. *Nat. Commun.* **12**, 2189 (2021).
36. Parat, F. & Holtz, F. Sulfur partitioning between apatite and melt and effect of sulfur on apatite solubility at oxidizing conditions. *Contrib. Mineral. Petrol.* **147**, 201–212 (2004).
37. Sadove, G., Konecke, B. A., Fiege, A. & Simon, A. C. Structurally bound S²⁻, S¹⁻, S⁴⁺, S⁶⁺ in terrestrial apatite: the redox evolution of hydrothermal fluids at the Phillips mine, New York, USA. *Ore Geol. Rev.* **107**, 1084–1096 (2019).
38. Konecke, B. A., Fiege, A., Simon, A. C., Parat, F. & Stechern, A. Co-variability of S⁶⁺, S⁴⁺, and S²⁻ in apatite as a function of oxidation state: Implications for a new oxybarometer. *Am. Mineral.* **102**, 548–557 (2017).
39. Konecke, B. A., Fiege, A., Simon, A. C., Linsler, S. & Holtz, F. An experimental calibration of a sulfur-in-apatite oxybarometer for mafic systems. *Geochim. Cosmochim. Acta* **265**, 242–258 (2019).
40. Bruand, E., Fowler, M., Storey, C. & Darling, J. Apatite trace element and isotope applications to petrogenesis and provenance. *Am. Mineral.* **102**, 75–84 (2017).
41. Bruand, E., Storey, C. & Fowler, M. An apatite for progress: inclusions in zircon and titanite constrain petrogenesis and provenance. *Geology* **44**, 91–94 (2016).
42. Meng, X. et al. Formation of oxidized sulfur-rich magmas in Neoproterozoic subduction zones. *Nat. Geosci.* **15**, 1064–1070 (2022).
43. Kemp, A. I. S. et al. Magmatic and crustal differentiation history of granitic rocks from Hf–O isotopes in zircon. *Science* **315**, 980–983 (2007).
44. Valley, J. W. Oxygen isotopes in zircon. *Rev. Mineral. Geochem.* **53**, 343–385 (2003).
45. Hiess, J., Bennett, V. C., Nutman, A. P. & Williams, I. S. In situ U–Pb, O and Hf isotopic compositions of zircon and olivine from Eoarchaean rocks, West Greenland: new insights to making old crust. *Geochim. Cosmochim. Acta* **73**, 4489–4516 (2009).
46. Loucks, R. R., Fiorentini, M. L. & Henríquez, G. J. New magmatic oxybarometer using trace elements in zircon. *J. Petrol.* **61**, egaa034 (2020).
47. Seixas, L. A. R., Bardintzeff, J. M., Stevenson, R. & Bonin, B. Petrology of the high-Mg tonalites and dioritic enclaves of the ca. 2130 Ma Alto Maranhão suite: evidence for a major juvenile crustal addition event during the Rhyacian orogenesis, Mineiro Belt, southeast Brazil. *Precambrian Res.* **238**, 18–41 (2013).
48. Seixas, L. A. R., David, J. & Stevenson, R. Geochemistry, Nd isotopes and U–Pb geochronology of a 2350 Ma TTG suite, Minas Gerais, Brazil: implications for the crustal evolution of the southern São Francisco craton. *Precambrian Res.* **196**, 61–80 (2012).
49. Moreira, H. et al. Evolution of siderian juvenile crust to rhyacian high Ba–Sr magmatism in the Mineiro Belt, southern São Francisco Craton. *Geosci. Front.* **9**, 977–995 (2018).
50. Spencer, C. J., Murphy, J. B., Kirkland, C. L., Liu, Y. & Mitchell, R. N. A Palaeoproterozoic tectono-magmatic lull as a potential trigger for the supercontinent cycle. *Nat. Geosci.* **11**, 97–101 (2018).
51. Cherniak, D. J. & Watson, E. B. Diffusion in zircon. *Rev. Mineral. Geochem.* **53**, 113–143 (2003).
52. Grimes, C. B., Wooden, J. L., Cheadle, M. J. & John, B. E. ‘Fingerprinting’ tectono-magmatic provenance using trace elements in igneous zircon. *Contrib. Mineral. Petrol.* **170**, 46 (2015).
53. Farquhar, J. & Wing, B. A. Multiple sulfur isotopes and the evolution of the atmosphere. *Earth Planet. Sci. Lett.* **213**, 1–13 (2003).
54. Canfield, D. E. et al. Petrographic carbon in ancient sediments constrains Proterozoic Era atmospheric oxygen levels. *Proc. Natl Acad. Sci. USA* **118**, e2101544118 (2021).
55. Lyons, T. W., Reinhard, C. T. & Planavsky, N. J. The rise of oxygen in Earth’s early ocean and atmosphere. *Nature* **506**, 307–315 (2014).
56. Cawood, P. A. & Hawkesworth, C. J. Temporal relations between mineral deposits and global tectonic cycles. *Geol. Soc. London Spec. Publ.* **393**, 9–21 (2015).

Publisher’s note Springer Nature remains neutral with regard to jurisdictional claims in published maps and institutional affiliations.

Open Access This article is licensed under a Creative Commons Attribution 4.0 International License, which permits use, sharing, adaptation, distribution and reproduction in any medium or format, as long as you give appropriate credit to the original author(s) and the source, provide a link to the Creative Commons license, and indicate if changes were made. The images or other third party material in this article are included in the article’s Creative Commons license, unless indicated otherwise in a credit line to the material. If material is not included in the article’s Creative Commons license and your intended use is not permitted by statutory regulation or exceeds the permitted use, you will need to obtain permission directly from the copyright holder. To view a copy of this license, visit <http://creativecommons.org/licenses/by/4.0/>.

© The Author(s) 2023

Methods

Sample preparation

Zircons were hand-picked and mounted on tape on a 5 × 5 mm area. A 25-mm-diameter round mount was then centred on top of the grains where epoxy resin was poured and dried in a vacuum chamber. The resin mounts were then polished to reveal the zircon interiors. Cathodoluminescence and backscatter electron images for U–Pb, oxygen and Lu–Hf analyses targeting were acquired at the University of Portsmouth. They show oscillatory zoning typical of magmatic grains^{24,49}. Host grains and inclusions were identified using elemental mapping by scanning electron microscopy-energy dispersive X-ray spectrometry. The spectral composition and ‘spot’ identification of the different phases were determined using a silicon drift (SDD-EDS) Oxford X-max 80 mm² detector attached to a SEM Zeiss EVO MA 10 LaB6 at the University of Portsmouth.

Synchrotron data acquisition and data processing

Sulfur speciation analyses were carried out using the ID21X-ray microscopy beamline at the ESRF in Grenoble, France⁵⁷. During the session, the sulfur speciation (S^{2-} , S^{4+} and S^{6+} and their proportions) was measured in both apatite grains and apatite inclusions in zircon. X-ray beam was produced using a 42-period undulator, and the energy was selected with a double-crystal monochromator. XANES spectra were acquired in the range of 2.46 to 2.53 keV, in continuous mode, with steps of 0.2 eV and 0.1 s per point, taking approximately 1 minute per point. The calibration of the double-crystal monochromator was done using a gypsum reference powder (maximum of white line of the XANES spectrum at 2.48184 keV). The fine tune and focusing was achieved using a set of two Kirkpatrick–Baez mirrors with a Ni coating. The beam was reduced to 0.3 μm V × 0.4 μm H. Sample mounts were mounted vertically in the microscope, and all measurements were carried out under vacuum (10⁻⁵ mbar). The beam was then used for construction of 2D μXRF elemental maps and μ-XANES spectra for chemical speciation. The detector used was an SGX 100 mm² SiriusSD silicon drift diode and a multichannel analyser. Dead time of the XRF detector was controlled, and beam intensity was attenuated so that dead time was always in the range of 17–22% throughout the session. XANES spectra were produced after correction by beam intensity (constantly measured with a photodiode upstream the sample) and the XRF dead time. Zircon host grains were analysed a few times to assess possible interferences. To separate the XRF K lines from S from the Zr L₂ and L₃ emissions lines, XRF spectra were batch fitted using the PyMca software⁵⁸. Inclusions were located thanks to μXRF map and appeared as ‘hotspot’ domains with high sulfur contents. To increase the signal to noise of XANES spectra, several points of interest were selected over each inclusion, and an average spectrum was obtained. This approach enables focusing the targets/regions rich in sulfur and optimizes the time spent for each sample.

The ESRF S K-edge XANES spectra inorganic database was used to identify the different peak energy positions for natural minerals with distinct sulfur speciation. To identify S^{6+} (-2,482 eV), S^{4+} (-2,478 eV) and S^{2-} (-2,470 eV), we used gypsum, pyrrhotite and pyrite. The high-focused beam yields high sulfur X-ray counts (in the order of ~6,000 counts per s for S^{6+} when measuring gypsum and ~4,500 counts per s for S^{2-} when measuring pyrite). The same Durango crystal analysed in ref. 38 was also analysed during the beginning and at the end of the session and the spectra was reduced as per the unknown apatites. As a similar procedure developed in ref. 38, we analysed across the grain perpendicularly to its *c* axis. Those comprise ten points measured twice each, testing homogeneity and beam damage. A single point at the core of the crystal was further analysed ten times and matched individual measurements, reassuring the minor existence of the beam damage for S^{6+} and S^{2-} peaks⁵⁹. Additionally, we analysed the same grain after a rotation of 90 degrees to assess the possible effect of the crystallographic orientation of the apatite. No differences were noticed in the spectra. The same experiment was performed with grain AMT_03_Zr12b

that contains inclusions 1 and 2. XANES data filtering and reduction was done using Python scripts and PyMca 5.5.5 software for visualization and selection of the reduction parameters. First, XANES spectra were filtered to exclude noisy spectra. Only spectra with a white line intensity that were at least two times higher than the signal measured at the pre-edge background were considered. XANES normalization values were 2.47006 keV for the edge and -0.008840, -0.004420 keV for pre-edge and 0.004550, 0.045496 keV for the post-edge. Spectra were fitted as a linear combination of Gaussian peaks, using a Python code and the advanced fitting from PyMca for Gaussians curves. Finally, the script extracted the peak area ratios (S^{6+}/S_{TOTAL}). The average integrated S^{6+}/S_{TOTAL} peak area ratio obtained for Durango is 0.956 ± 0.004 (2 standard error), in agreement with the peak area ratio obtained in ref. 38 (0.956 ± 0.002 ; 2 standard error).

Electron backscatter diffraction

Electron backscatter diffraction (EBSD) analyses were performed in zircon, apatite and apatite inclusions to evaluate the microstructural relationship of these phases and the possible relationship between sulfur speciation and crystallographic orientation. Analyses were performed at Géosciences Montpellier, France, using a CamScan X500-FEG Crystal Probe. This SEM was developed from its conception for high-resolution crystallographic mapping by backscattered electron diffraction. It thus has the particularity of having its electronic column tilted at 70°, which makes it possible to keep the sample horizontal during analyses, and allows backscattered electron diffraction detection of surfaces with uneven polishing. The EBSD Symmetry detector of CMOS technology was used for crystallographic analysis and a detector EDS UltimMax 100 was used for chemical analysis. Reduction of the data was performed using the AZtec software of Oxford Instruments. The crystallographic data were processed using *Tango* for orientation map display. Noise reduction was applied to the raw crystallographic data and the final EBSD maps contain the band contrast for quality of the diffraction pattern and lattice orientation of each phase analysed. Within each phase analysed, no misorientation >3° was observed, suggesting high crystallinity of individual phases and that processes of recrystallization are unlikely to have occurred. The small misorientation observed is possibly caused by polishing and hardness of the apatite inclusions against the zircon host. Nonetheless, these features do not compromise the refraction of part of the inclusions and are sufficient enough quality to assess crystallographic orientation. We analysed apatite inclusions with variable crystallographic orientations, which show no correlation in their sulfur μ-XANES spectra (Fig. 2).

Zircon trace element analysis

Trace element composition was obtained by laser ablation inductively coupled plasma mass spectrometry on distinct zircon domains. Analyses were conducted using an ASI RESOLUTION Excimer 193 nm laser system, coupled to an Analytik Jena PlasmaQuant Elite ICP-MS at the University of Portsmouth, United Kingdom. Laser ablation settings for the first session were 30 μm, 3 Hz and 3.5 J cm⁻². Analyses were located on top of previous electron microprobe or U–Pb analyses. Oxide formations in the plasma were estimated by monitoring the ThO⁺/Th⁺ and UO⁺/U⁺ on the National Institute of Standards and Technology (NIST) glass standard reference material 612, and tuning was done to reach values below 0.3% and 0.2% for the ThO⁺/Th⁺ and UO⁺/U⁺ ratios, respectively. Elemental fractionation was monitored through repeated measurements of the ²³²Th/²³⁸U ratio in NIST 612, with variations between 0.9 and 1 observed during analytical sessions. The carrier gas flow in the ablation cell was set to 0.310 l min⁻¹ and combined with 0.003 l min⁻¹ of N₂ gas before introduction to the ICP. Plasma generation was set at 1,300 W with 10 l min⁻¹ of Ar plasma flow, auxiliary gas flow of 1.65 l min⁻¹ and nebulizer flow between 0.89 and 0.9 l min⁻¹. The glass NIST 612 was used as a primary standard and zircon reference materials 91500⁶⁰, GJ-1^{61,62}, Plešovice⁶³ and Temora-2⁶⁴ were used as secondary

standards. The glass NIST 612 was analysed four times at the beginning and at the end of the session and twice each group of unknowns. Each group of unknowns consisted of a combination of four investigated zircons and two secondary standards. The following isotopes were measured and had an integration time of 10 ms: ^{25}Mg , ^{27}Al , ^{29}Si , ^{31}P , ^{39}K , ^{43}Ca , ^{45}Sc , ^{49}Ti , ^{51}V , ^{53}Cr , ^{55}Mn , ^{85}Rb , ^{87}Sr , ^{89}Y , ^{90}Zr , ^{93}Nb , ^{95}Mo , ^{118}Sn , ^{121}Sb , ^{133}Cs , ^{137}Ba , ^{139}La , ^{140}Ce , ^{141}Pr , ^{146}Nd , ^{147}Sm , ^{153}Eu , ^{157}Gd , ^{159}Tb , ^{163}Dy , ^{165}Ho , ^{166}Er , ^{169}Tm , ^{172}Yb , ^{175}Lu , ^{178}Hf , ^{181}Ta , ^{182}W , ^{208}Pb , ^{209}Bi , ^{232}Th , ^{238}U . The raw data were reduced and corrected for instrumental drift using the Lolite 3.4 software⁶⁵. Zirconium content was used for internal calibration and measured using a Cameca SX100 electron microprobe at the University of Bristol, United Kingdom (below), avoiding using stoichiometry when normalized. NIST 610 and secondary zircon reference materials yielded results within 10–15% in accuracy relative to the recommended published values.

Pressure and temperature dependence

Experimental studies in silicate melts demonstrate that an increase in 100 °C temperature imparts a $\Delta\text{FMQ} - 0.5$ deviation in the magma f_{O_2} ; whereas an increase in 0.3 GPa would impart a $\Delta\text{FMQ} + 0.2$ deviation^{66,67}. Direct measurement of temperature crystallization via Ti-in-zircon thermometry⁶⁸ indicates that zircon grains from the sanukitoid samples crystallized at 800 ± 13 °C (2 standard error), and TTG samples have zircons with average crystallization temperature of 700 ± 10 °C (2 standard error), considering SiO_2 and TiO_2 activity = 1. A lower TiO_2 activity such as 0.7 yields higher temperatures of crystallization, 839 °C and 726 °C, respectively, for sanukitoid and TTG zircons. Al-in-hornblende oxybarometer indicates crystallization pressures at around 0.6–0.4 GPa for the sanukitoid samples⁴⁷, whereas higher pressure conditions were suggested for the TTG samples (-0.7 GPa) based on the presence of igneous almandine garnet and overall trace element modelling⁴⁸. The -0.3 GPa difference in pressure between these two magmatic suites is not enough to explain a > 1.0 ΔFMQ difference between the calculated f_{O_2} for sanukitoid and TTG magmas. Moreover, the -100 °C difference in temperature, if considered, would amplify the contrast in fugacity obtained via sulfur oxybarometry.

Electron probe microanalysis

Zircon grains were analysed by electron probe microanalysis at the University of Bristol, United Kingdom, using a Cameca SX100. An electron beam of 5 μm was used with an acceleration voltage of 17 kV and 100 nA beam current. Element concentrations (Si, P, Y, Zr, Yb, Lu, Th and Hf) were determined using thallium acid phthalate, large pentaerythritol, large lithium fluoride and pentaerythritol crystals. The 91500 zircon standard⁶⁰ was analysed during the microprobe sessions to monitor data quality. Only analyses with concentrations more than the sum of the individual detection limit and the absolute 2σ error were considered. The Zr content was used for internal calibration of trace element analyses presented above and vary from 47 to 48%.

Data availability

Supporting information for this study is available at <https://doi.org/10.6084/m9.figshare.22738082>.

Code availability

PyMca 5.5.5 (<http://www.silx.org/doc/PyMca/dev/index.html>) and Python scripts (<https://zenodo.org/deposit/7693613>) were used for data visualization and reduction.

References

57. Cotte, M. et al. The ID21 X-ray and infrared microscopy beamline at the ESRF: status and recent applications to artistic materials. *J. Anal. At. Spectrom.* **32**, 477–493 (2017).

58. Solé, V. A., Papillon, E., Cotte, M., Walter, P. & Susini, J. A multiplatform code for the analysis of energy-dispersive X-ray fluorescence spectra. *Spectrochim. Acta B* **62**, 63–68 (2007).
59. Wilke, M. et al. The origin of S^{4+} detected in silicate glasses by XANES. *Am. Mineral.* **93**, 235–240 (2008).
60. Wiedenbeck, M. A. P. C. et al. Three natural zircon standards for U-Th-Pb, Lu-Hf, trace element and REE analyses. *Geostand. Newsl.* **19**, 1–23 (1995).
61. Jackson, S. E., Pearson, N. J., Griffin, W. L. & Belousova, E. A. The application of laser ablation-inductively coupled plasma-mass spectrometry to in situ U–Pb zircon geochronology. *Chem. Geol.* **211**, 47–69 (2004).
62. Piazzolo, S., Belousova, E., La Fontaine, A., Corcoran, C. & Cairney, J. M. Trace element homogeneity from micron-to atomic scale: implication for the suitability of the zircon GJ-1 as a trace element reference material. *Chem. Geol.* **456**, 10–18 (2017).
63. Schoene, B., Latkoczy, C., Schaltegger, U. & Günther, D. A new method integrating high-precision U–Pb geochronology with zircon trace element analysis (U–Pb TIMS-TEA). *Geochim. Cosmochim. Acta* **74**, 7144–7159 (2010).
64. Black, L. P. et al. Improved $^{206}\text{Pb}/^{238}\text{U}$ microprobe geochronology by the monitoring of a trace-element-related matrix effect; SHRIMP, ID-TIMS, ELA-ICP-MS and oxygen isotope documentation for a series of zircon standards. *Chem. Geol.* **205**, 115–140 (2004).
65. Paton, C., Hellstrom, J., Paul, B., Woodhead, J. & Hergt, J. Lolite: freeware for the visualisation and processing of mass spectrometric data. *J. Anal. At. Spectrom.* **26**, 2508–2518 (2011).
66. Matjuschkin, V., Blundy, J. D. & Brooker, R. A. The effect of pressure on sulphur speciation in mid-to deep-crustal arc magmas and implications for the formation of porphyry copper deposits. *Contrib. Mineral. Petrol.* **171**, 66 (2016).
67. Nash, W. M., Smythe, D. J. & Wood, B. J. Compositional and temperature effects on sulfur speciation and solubility in silicate melts. *Earth Planet. Sci. Lett.* **507**, 187–198 (2019).
68. Ferry, J. M. & Watson, E. B. New thermodynamic models and revised calibrations for the Ti-in-zircon and Zr-in-rutile thermometers. *Contrib. Mineral. Petrol.* **154**, 429–437 (2007).

Acknowledgements

This project was funded by the European Research Council under the European Union's Horizon 2020 research and innovation programme (number 817934) and CNPq (National Council for Scientific and Technological Development) grant (234610/2014-0) to H.M. P.P. acknowledges support from the São Paulo Research Foundation (FAPESP 2015/16235-2). We acknowledge the European Synchrotron Radiation Facility for provision of synchrotron radiation facilities through proposal ES-942. We thank F. Barou for assistance with EBSD analyses.

Author contributions

H.M. and C.S. conceived the idea. H.M. performed electron probe and laser ablation analyses. H.M., C.S., E.B., J.D. and B.D. wrote the synchrotron proposal and acquired XANES data. M.F. provided guidance on secular magmatic evolution and sediment–mantle interactions. M.C. coordinated the synchrotron session and validated methodology and data reduction. E.E.V.-P. developed the code and reduction protocols for XANES. F.P. provided standards for XANES, conceptual guidance and interpretation of sulfur speciation analysis. L.S. provided fieldwork guidance and validation of the study. P.P. validated interpretations about atmospheric interactions. Original draft was written by H.M. with input and edits from all authors.

Competing interests

The authors declare no competing interests.

Additional information

Supplementary information The online version contains supplementary material available at <https://doi.org/10.1038/s41561-023-01258-4>.

Correspondence and requests for materials should be addressed to Hugo Moreira.

Peer review information *Nature Geoscience* thanks Robert Nicklas and Adam Simon for their contribution to the peer review of this work. Primary Handling Editors: Louise Hawkins, Alison Hunt and James Super, in collaboration with the *Nature Geoscience* team.

Reprints and permissions information is available at www.nature.com/reprints.